Catalysis Science & Technology

ROYAL SOCIETY OF CHEMISTRY

PAPER

View Article Online
View Journal | View Issue

Cite this: *Catal. Sci. Technol.*, 2021, 11, 5282

Reaction pathways and deactivation mechanisms of isostructural Cr and Fe MIL-101 during liquid-phase styrene oxidation by hydrogen peroxide†

Rachel A. Yang and Michele L. Sarazen *

Isostructural Cr and Fe nanoporous MIL-101, synthesized without mineralizing agents, are investigated for styrene oxidation utilizing aqueous hydrogen peroxide to yield valuable oxygenates for chemical synthesis applications. Styrene conversion rates and oxygenate product distributions both depend on metal identity, as MIL-101(Fe) is more reactive for total styrene oxidation and is more pathway selective, preferring aldehyde (benzaldehyde) formation at the α-carbon to the aromatic ring, where MIL-101(Cr) sustains epoxide (styrene oxide) production at the same α-carbon. These pathways often involve hydrogen peroxide derived radical intermediates (=O, –HOO•, –HO•) and metallocycle transition states. We postulate that the higher reactivity of one of these surface intermediates, Fe(IV)=O relative to Cr(IV)=O, leads to higher styrene oxidation rates for MIL-101(Fe), while higher electrophilicity of Cr(III)–OOH intermediates translates to the higher styrene oxide selectivity observed for MIL-101(Cr). Secondary styrene oxide and benzaldehyde conversions are observed over both analogs, but the former is more prevalent over MIL-101(Fe) due to higher Lewis/Brønsted acid site density and strength compared to MIL-101(Cr). Recyclability experiments combined with characterization *via* XRD, SEM/EDXS, and FT-IR and UV-vis spectroscopies show that the nature of MIL-101(Fe) sites does not change significantly with each cycle, whereas MIL-101(Cr) suffers from metal leaching, which impacts styrene conversion rates and product distribution. Both catalysts require active site regeneration, though MIL-101(Fe) sites are more susceptible to reactivation, even under mild conditions. Finally, examination of styrene conversion for three unique synthesized phases of MIL-101(Cr) rationalizes that nodal defects are largely responsible for observed reactivity and selectivity but predispose the framework to metal leaching as a predominant deactivation mechanism.

Received 31st March 2021,
Accepted 30th June 2021

DOI: 10.1039/d1cy00567g

rsc.li/catalysis

Introduction

Metal–organic frameworks (MOFs) are a class of crystalline, porous solids that have garnered attention by merit of their modular and attractive physiochemical properties. They have been investigated for diverse applications including gas separation and storage,[1] water purification,[2] drug delivery,[3] sensing,[4,5] nonlinear optics,[6] and catalysis.[7–10] In the context of catalysis, MOFs have exhibited activity for small-molecule transformations including the carbonation of light alkenes,[11–13] Friedel–Crafts reactions,[14] cross-coupling reactions,[15] and the oxidation of aromatic and linear hydrocarbons.[16–18]

Here, we focus on MOF-catalyzed oxidation reactions, motivated by the prevalence of this class of transformations in pharmaceutical, fine chemical, and other hydrocarbon valorization applications. Many of these processes are performed in liquid-phase, batch systems and utilize transition metal molecular catalysts, which have some unfavorable economical and sustainability attributes, such as additional separation costs and challenges in regeneration for reuse in subsequent reaction cycles. Though there are some notable examples of recyclable homogeneous catalysts for aryl and alkyl oxidations,[19–21] generally, industrial application of homogeneous catalysts is still limited by costly separations needed for catalyst recovery. As such, we investigate MOFs as solid analogs for transition metal organometallics in heterogeneous liquid-phase, small-molecule organic oxidations. A subset of these nanoporous (<100 nm) networks have demonstrated notable reactivity and selectivity for the oxidations of some alkyl and aryl alkenes by benign oxidants like hydrogen peroxide (H_2O_2) and air.[7,9,17,22] However, widespread MOF use is marred by thermochemical instability relative to more conventional porous materials like bulk metal oxides and zeolites. One exception is the MIL-101 family, which includes some transition metal variants that are both active for oxidative

Department of Chemical and Biological Engineering, Princeton University, Princeton, New Jersey 08544, USA. E-mail: msarazen@princeton.edu

† Electronic supplementary information (ESI) available. See DOI: 10.1039/d1cy00567g

chemistry and are stable in air (up to 548 K), water, and many common polar and nonpolar solvents.[7,22,23] Further, it is a higher surface area material unlike most bulk metal oxides and does not suffer from limited pore size ranges and fast deactivation in liquid-phase reactions due to poisoning, pore occlusion, and severe metal leaching unlike zeolites.[17,22]

The oxidation of styrene by hydrogen peroxide is selected as a probe reaction for the value of its oxygenate products in chemical synthesis applications and for its green appeal, since hydrogen peroxide is a cleaner oxidant compared to organic peroxides, which often have toxic byproducts.[17] Further, this system affords an opportunity to probe metal-oxidant interactions, reactivity, and material stability in an oxidizing environment that can accelerate catalytic/metal cycles. The complex nature of the involved reaction pathways can probe different sites and defects within the model MIL-101 family that can be extended to other small-molecule organic oxidations on isolated-site transition metal catalysts. Structurally, MIL-101 is a nanoporous solid comprised of metal oxide trimer node species ($[M_3O(OH)_3]^{n+}$) coordinated to 1,4-benzene dicarboxylic acid (BDC) linkers that assemble to form an MTN zeotype crystal structure (Fig. 1) with 3.4 nm cages accessible by 1.6 nm hexagonal windows and smaller 2.9 nm cages accessible by 1.2 nm pentagonal windows.[23] This large (mesoporous) and accessible pore network tends to mitigate diffusion-limited reactions for a wide range of substrates, as larger pores allow more facile access to internal active sites. Further, its ordered network with well-defined active site location and nature facilitates a more controlled study of site evolution during catalytic cycles. This family is synthetically diverse, including chromium, iron, vanadium, and titanium analogs, some of which have established activity for various catalytic alkyl and aryl oxidation reactions in the liquid-phase at mild reaction conditions.[16,17,24–27] However, precise reaction pathways and deactivation mechanisms are still elusive for many MOF-catalyzed oxidation systems. As such, this work investigates a probe liquid-phase aryl oxidation over transition metal MIL-101 to elucidate catalyst reactivity and pathways, physicochemical property evolution to reveal deactivation mechanisms, and active site recyclability, which is broadly important for efficient material use.

Here, we focus on MIL-101(Fe) and MIL-101(Cr) because they contain earth-abundant transition metal sites and have demonstrated activity for styrene oxidation,[17] as well as other small-molecule organic oxidations,[16,24,28] by a variety of oxidants like H_2O_2, air, and *t*-butyl hydrogen peroxide (TBHP). Moreover, MIL-101(Fe) and MIL-101(Cr) reportedly do not suffer from the same extensive metal leaching[17] that is observed with V-based MOFs or from inactivity observed with Ti-based MOFs during cyclic alkene oxidation.[27] Metal leaching has been reported for MIL-101(Cr) and MIL-101(Fe) in the presence of H_2O_2,[29] but the impacts on catalytic activity have not been thoroughly quantified. It has been observed that styrene oxidation at mild reaction conditions (353 K) on both MIL-101(Cr) and MIL-101(Fe) have the highest epoxide selectivity when TBHP is used, followed by air and H_2O_2.[17] Selectivity to other oxygenates is also impacted by oxidant identity, as are styrene conversion trends. MIL-101(Fe) shows higher styrene conversion for air > TBHP > H_2O_2 in contrast to H_2O_2 > air > TBHP for MIL-101(Cr).[17] This suggests that there are underlying textural and electronic differences between these two analogs that potentially manifest in different mechanisms. Yet, these underlying properties and their implications for MOF-catalyzed aromatic oxidation reaction pathways are neither well understood nor quantified, even though existing literature has found differences in catalytic activity between

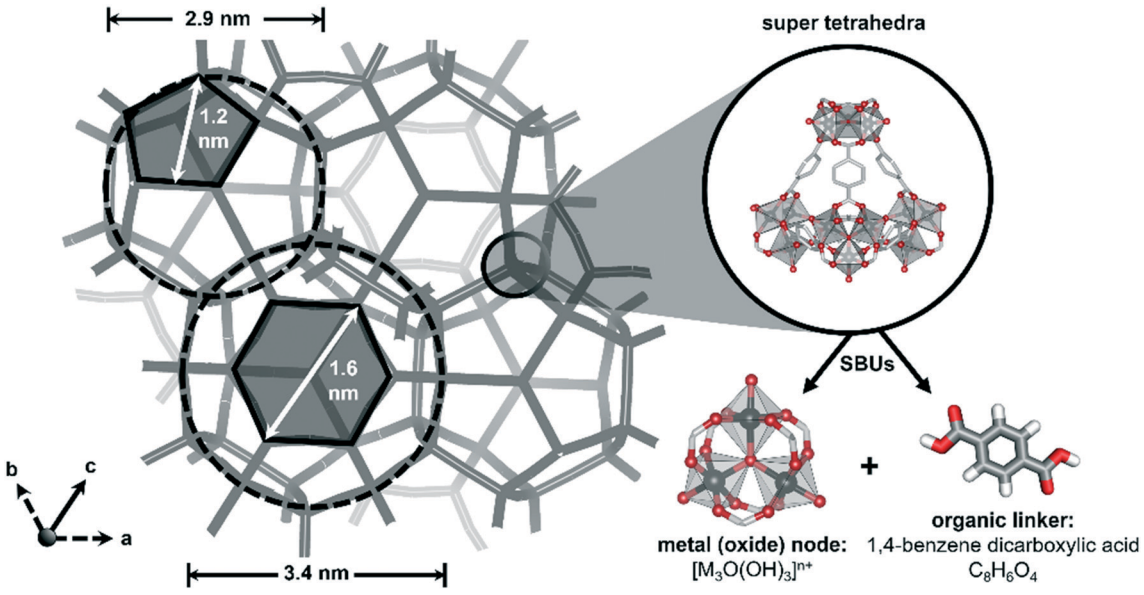

Fig. 1 MIL-101(M) nanoporous MTN-zeotype framework with trimeric metal node structure and organic linker secondary building units (SBUs) with nominal chemical formulas.

these two isostructural frameworks for a handful of other liquid-phase small molecule oxidations.[25,28] Further, there is a dearth of studies that go beyond assessment of activity in terms of conversion or quantitatively investigate deactivation mechanisms for MOF-catalyzed oxidation reactions. These mechanisms are imperative to understanding material limitations that arise under realistic reaction conditions, to proposing deactivation mitigation strategies, and to providing a thorough basis for comparison for future synthetic efforts to improve material stability. Overall, this work examines isostructural MIL-101(Cr) and MIL-101(Fe) frameworks to rationalize the effects of metal identity and other intrinsic material properties on MOF-catalyzed oxidation pathways and elucidates deactivation mechanisms with rigorous quantification of turnover rates and product distributions to define the efficacy and limitations of these novel transition metal catalysts through their life cycles for styrene oxidation by hydrogen peroxide, a representative aryl oxidation.

Experimental

Materials and methods

1,4-Benzene dicarboxylic acid (BDC, Acrōs Organics, 99+%), iron(III) chloride hexahydrate ($FeCl_3{\cdot}6H_2O$, Acrōs Organics, 99%), chromium(III) nitrate nonahydrate ($Cr(NO_3)_3{\cdot}6H_2O$, Acrōs Organics, 99%), *N*,*N*-dimethylformamide (DMF, Fisher Chemical, 99.9%), ethanol (EtOH, Fisher Chemical, 97%), methanol (MeOH, J.T. Baker, 99.9%), and acetone (VWR Chemicals, 99.5%) were used for synthesis of MIL-101(Fe) and MIL-101(Cr). Styrene (stabilized, Acrōs Organics, 99.5%), acetonitrile (CH_3CN, Honeywell Riedel-de Haën, 99.7+%), and hydrogen peroxide (H_2O_2, Fisher Chemical, 30% v/v in H_2O) were used for catalytic experiments. Deuterated dimethyl sulfoxide (DMSO-d_6, Cambridge Isotope Laboratories, 99.9%) was used as the solvent for ^{1}H NMR analysis. All starting materials and organic solvents were used as received without further purification. MIL-101(Cr) and MIL-101(Fe) were synthesized without the use of toxic mineralizing agents like hydrofluoric acid (HF), following published literature procedures with some modifications.[16,30]

Typical synthesis of MIL-101(Cr)

MIL-101(Cr) was synthesized by first mixing equimolar (5 mmol) chromium(III) nitrate nonahydrate and BDC in 24 mL deionized water at ambient temperature and pressure. The acidic dark indigo suspension was sonicated for 10 minutes before it was charged into a 45 mL Teflon-lined stainless-steel Parr autoclave and put into a convection isothermal oven at 491 K for 18 hours at autogenous pressure without stirring. The mixture was cooled naturally to ambient temperature. Afterward, the solids were separated by centrifugation (5000 × *g*, 10 min) and washed with water, methanol, and acetone in succession. The remaining solid was separated from acetone *via* centrifugation, introduced to 20 mL DMF, sonicated for 10 minutes, and kept at 343 K overnight without stirring. The emerald-green solid was separated by centrifugation, washed with methanol and acetone sequentially, dried at 348 K overnight and then in vacuum (125 torr) at ambient temperature for 2 days. Typical yield of the emerald-green solid was 14% by mass on a Cr basis with a nominal chemical formula of $[Cr_3(O)(OH)(BDC)_3(H_2O)_2]$.

Typical synthesis of MIL-101(Fe)

In a typical synthesis of MIL-101(Fe), 2.45 mmol of iron(III) chloride hexahydrate and 1.24 mmol of BDC were mixed in 15 mL of DMF until clear with a goldenrod-yellow color. The mixture was sonicated for 15 minutes and then charged into a 23 mL Teflon-lined stainless-steel Parr autoclave. The autoclave was heated at 383 K for 20 hours and after cooling to ambient temperature naturally, the resulting red-orange solid was collected *via* centrifugation (1000 × *g*, 5 min). The solid was washed two times, 3 hours each, with ethanol at 333 K under refluxing conditions. The purified orange product was separated *via* vacuum filtration and dried at 343 K overnight. Typical yield of the orange solid was 32% by mass on an Fe basis with a nominal chemical formula of $[Fe_3(O)(Cl)(BDC)_3(H_2O)_2]$.

Catalyst characterization

Powder X-ray diffraction (XRD) patterns were obtained on a Bruker D8 Discover diffractometer with Cu-Kα radiation (λ = 1.5418 Å) operating at 40 kV and 40 mA. Images were procured using an XL30 field emission gun scanning electron microscope (SEM) and an Evex energy dispersive X-ray spectroscopy (EDXS) accessory was used to determine approximate elemental composition and for elemental mapping. A Nicolet iS50 infrared spectrophotometer was used to gather spectra for all materials; all solid samples (2 wt%) were mixed with KBr and pressed into pellets utilizing a hydraulic press at 11 000 psi for 5 minutes each. UV-vis spectroscopy was used to analyze both liquid samples and solid suspensions and measurements were performed on an Agilent Technologies Cary 5000 UV-vis-NIR spectrophotometer. Multipoint Brunauer–Emmett–Teller (BET) surface area and non-local density functional theory (NLDFT) pore size measurements were calculated from N_2 adsorption and desorption isotherms (77 K) collected on a Micromeritics 3Flex physisorption unit. The pressure (P/P_0) ranges used for BET surface area calculations were chosen to satisfy the maximum number of consistency criterion[31] and typical ranges were 0.05 to 0.18 for MIL-101(Cr) and 0.01 to 0.15 for MIL-101(Fe). The N_2-Tarazona NLDFT model with cylindrical geometry was used for pore size distributions. All samples were degassed at 383 K under mild vacuum (125 torr) overnight prior to N_2 physisorption unless stated otherwise. A Micromeritics Autochem II 2920 was used to perform temperature programmed desorption (TPD) measurements utilizing NH_3 and CO_2, as detailed in the supporting information.

Catalytic styrene oxidation by hydrogen peroxide

Reaction–reactivation cycling experiments were conducted at 323 K in 100 mL round-bottom flasks under refluxing conditions with a starting broth composition of 10 mL acetonitrile, 10 mmol styrene, and 30 mmol hydrogen peroxide. 50 mg of catalyst was subsequently added to initiate the reaction. After 3600 s (1 h), the solid was separated using centrifugation (1000 × *g*, 5 min) and a 20 μL aliquot of the liquid supernatant was mixed thoroughly in DMSO-d_6 for analysis *via* ^{1}H NMR on a Bruker 500 MHz spectrometer. Resulting spectra were integrated and the areas were utilized to calculate styrene conversion and product selectivities on a fractional basis. All spectra were repeatedly integrated, and associated error was calculated from standard deviations of these integrated areas; error was propagated appropriately with each functional transformation. The recovered solid was reactivated by washing with acetonitrile and ethanol in succession and then drying under mild vacuum conditions overnight (125 torr). The resulting solid was then retested for catalytic activity in fresh reaction medium. Temporal experiments were run similarly, with a 50 mg initial catalyst charge, but liquids were scaled up by a factor of 5 (50 mL acetonitrile, 50 mmol styrene, 150 mmol H_2O_2) with respect to the cycling experiment broths so that aliquots (20 μL) taken at various time points did not significantly impact the total solution volume.

Hot filtration tests were performed with the same starting broth composition as the cycling experiments, but after 3600 s of reaction, the solid was removed *via* vacuum filtration and the warm filtrate was quickly reintroduced to a fresh 100 mL reaction flask at temperature. The filtrate was allowed to react for another 3600 s and then a 20 μL aliquot was taken for ^{1}H NMR analysis.

Results and discussion

Textural characterization of catalytic materials

XRD patterns (Fig. 2a) for MIL-101(Cr) and MIL-101(Fe) show characteristic framework peaks that are consistent with those reported in literature and with the simulated pattern for a defect-free crystal with long-range translational order acquired from RIETAN-FP in VESTA.[16,30,32] FT-IR spectra (Fig. 2b) for both materials exhibit characteristic symmetric and asymmetric stretching modes of O–C–O functionalities in the 1400 to 1600 cm^{-1} range, aromatic C=C stretching vibrations near 1500 cm^{-1}, and C–H in-plane bending vibrations at approximately 1160 and 1020 cm^{-1} and out-of-plane bending at around 885 and 750 cm^{-1}.[32–34] The Fe analog has an additional band at 550 cm^{-1}, which is typical for a MIL-101 Fe–O stretch.[35] Since Cr–O has a lower reduced mass than Fe–O (12.2 g *versus* 12.4 g), the band at 587 cm^{-1} is likely the analog Cr–O vibration, as this band is also observed in Cr(III) oxide;[36] however, this band has not been assigned formally in MIL-101 literature to our knowledge despite being present. That assignment aside, all aforementioned bands are consistent with the MIL-101 framework and provide further evidence of successful syntheses of both analogs with functionalities comparable to other reported materials.[17] From SEM images (Fig. 2c and d), both analogs have self-consistent, well-defined crystal aggregate geometry and size distributions (Fig. S3†) centered at 0.31 ± 0.09 μm and 1.2 ± 0.3 μm for MIL-101(Cr) and MIL-101(Fe), respectively; this size disparity is a result of different synthetic conditions from the available literature procedures used for each material.[30,32] For example, hydrothermal synthesis for MIL-101(Cr) starts with a metal : linker : solvent molar ratio of 1 : 1 : 222 whereas solvothermal synthesis in DMF for MIL-101(Fe) starts with a ratio of 2 : 1 : 156. These differences, in addition to higher temperatures and shorter times for MIL-101(Cr) synthesis (491 K, 18 h) compared to MIL-101(Fe) synthesis (383 K, 20 h), likely impact crystal nucleation and growth rates. EDXS elemental mapping (Fig. S5a and S6†) indicates that the Cr (12.8 at%) and Fe (6.6 at%) are distributed throughout MIL-101(Cr) and MIL-101(Fe), respectively. This, combined with the lack of Cr and Fe oxide peaks in XRD patterns (Fig. S2†), suggests that

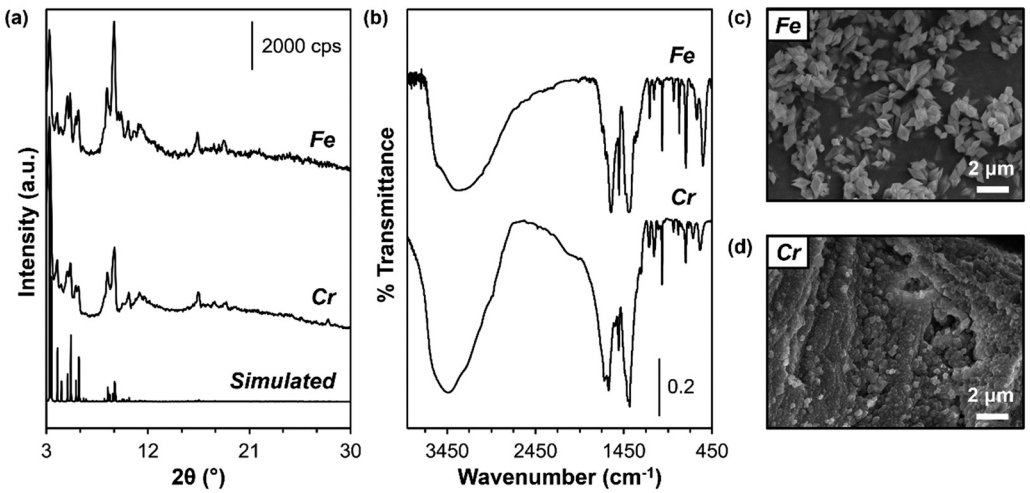

Fig. 2 (a) MIL-101(Cr, Fe) XRD patterns with simulated MIL-101 pattern, (b) FT-IR spectra of MIL-101(Cr, Fe), and SEM images of (c) MIL-101(Fe) and (d) MIL-101(Cr).

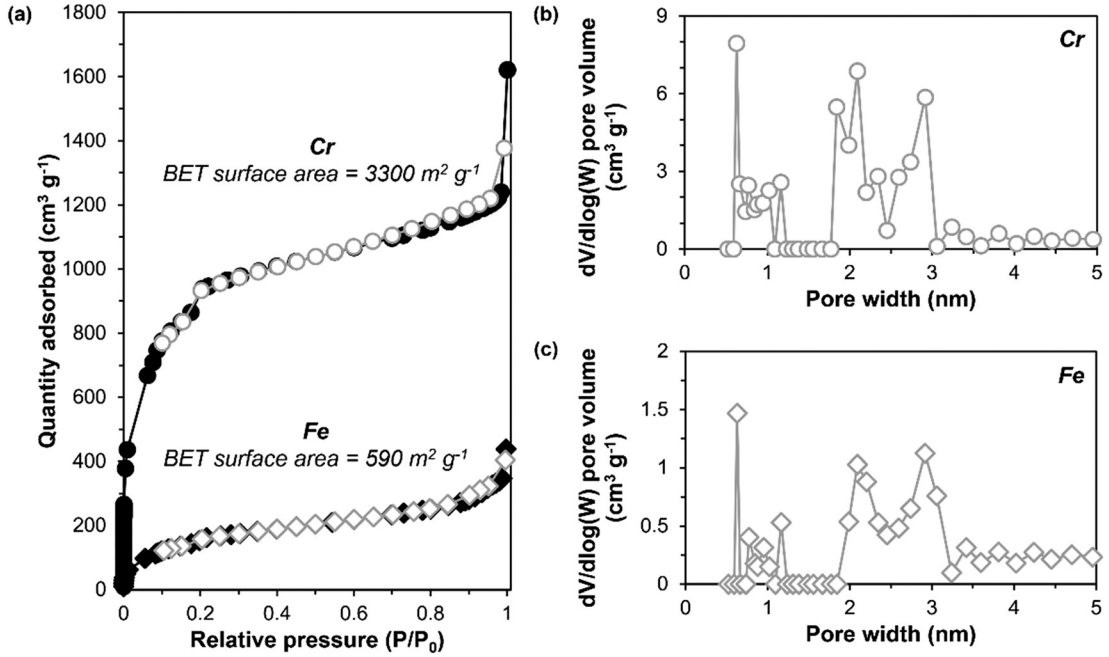

Fig. 3 (a) N_2 adsorption (Cr (black circles), Fe (black diamonds)) and desorption (Cr (grey circles), Fe (grey diamonds)) isotherms at 77 K and multipoint BET surface areas. NLDFT PSD for (b) MIL-101(Cr) and (c) MIL-101(Fe).

neither material forms large metallic or metal oxide clusters.

N_2 physisorption measurements at 77 K (Fig. 3a) result in high multipoint BET surface area, 3300 ± 50 m^2 g^{-1} for MIL-101(Cr) and 590 ± 10 m^2 g^{-1} for MIL-101(Fe). MIL-101(Fe), however, was found to exhibit lower BET surface areas (150–500 m^2 g^{-1}) when degassed at 383 K and 125 torr overnight, seemingly because the harsher procedure leads to partial collapse of pores due to strong capillary forces associated with solvent evacuation[37,38] (Fig. S7†). As such, milder degassing conditions (313 K, 125 torr for 2 days) were adopted and yielded higher surface area measurements (Fig. 3a and S8a†). Differences in literature purification and activation procedures[16,17,32] may also be implicated for lower surface area MIL-101(Fe); insufficient washing solvent volume or washing with solvents that exhibit low impurity solubility allows pervasive occluding species, including unreacted starting materials and amorphous Fe-BDC phases, to remain in the pores. Meanwhile, subsequent thermal or reduced pressure activation to remove washing solvent molecules from material pores may lead to occluded residual solvent, if the treatment is too mild, or collapse of pores, if the treatment is too harsh.[37–39] NLDFT pore size distributions (PSD), based on N_2 physisorption, demonstrate that MIL-101(Cr) (Fig. 3b) has micropore diameters in the 0.6–1.1 nm range and mesopore diameters in the 1.9–2.9 nm range, which are consistent with literature PSDs for this analog.[17] The former range is attributed to the microporous super tetrahedra (Fig. 1), whilst the latter range represents framework cages.[40] Similarly, high surface area (>500 m^2 g^{-1}) MIL-101(Fe) (Fig. 3c) has dimensions in the microporous range of 0.6–1.0 nm and sharply defined mesopore diameters in the 2.1–2.9 nm range. Lower surface area MIL-101(Fe) samples (<300 m^2 g^{-1}) show no microporosity and very broad mesopore distribution whereas intermediate samples (300 m^2 g^{-1} < x < 500 m^2 g^{-1}) retain some microporosity but start to show less defined mesopore distributions with increased broadening (Fig. S7†). However, we note that experimental conditions for N_2 physisorption are not representative of the pretreatments or liquid-phase environments employed in the following catalytic studies and instead serve as a means to compare synthesized materials to literature. In fact, two samples of MIL-101(Fe) with nearly identical textural properties that showed BET surface areas of 590 ± 10 m^2 g^{-1} and 860 ± 10 m^2 g^{-1} showed identical catalytic performance, as measured by turnover rates and product distribution (Fig. S19 and S20†). Overall, the MIL-101(Fe) and MIL-101(Cr) syntheses were successful in producing high surface area, crystalline materials to be utilized in the following catalytic experiments.

Temporal experiments and the examination of reaction pathways

Temporal fractional styrene conversion (Fig. 4a) and oxygenate concentration profiles (Fig. 4b and c) are first obtained to define the reactivity of each analog. Styrene conversion is higher for MIL-101(Fe) compared to MIL-101(Cr) at all time points for the same initial charge of catalyst on a total mass basis. Reactivity for styrene oxidation for MIL-101(Fe) is also higher relative to MIL-101(Cr), as determined from pseudo first-order reaction rates normalized by initial catalyst mass loadings and by moles of metal determined from EDXS. Further, oxygenate concentration

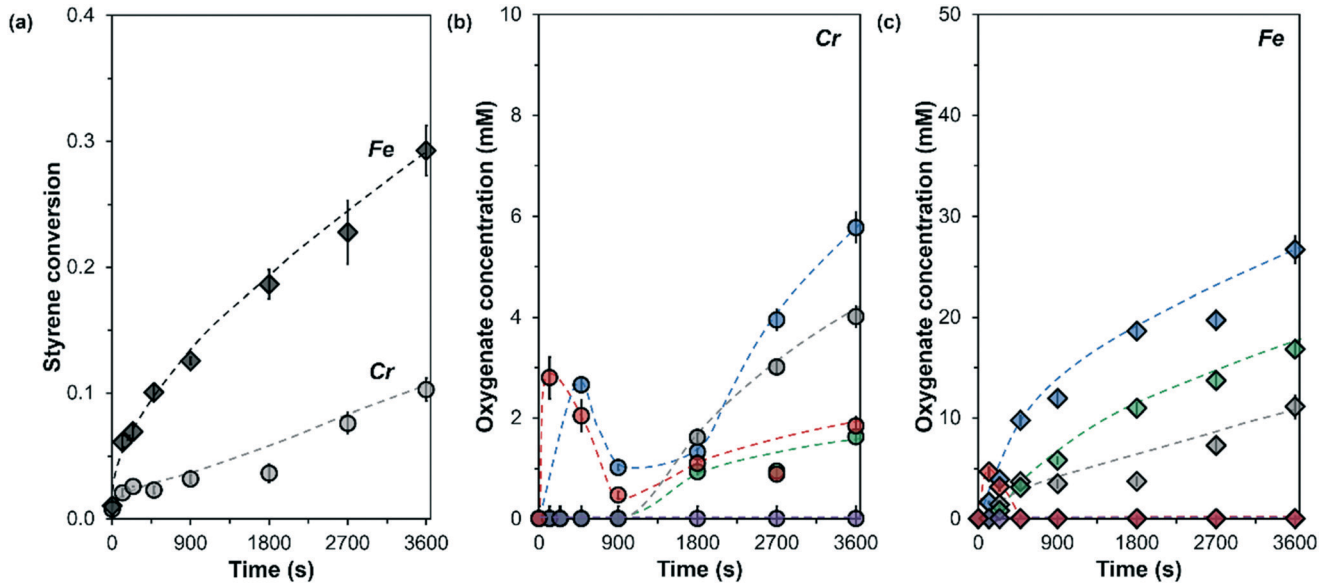

Fig. 4 Temporal (a) fractional styrene conversion for MIL-101(Cr) (grey) and MIL-101(Fe) (black) and oxygenate (styrene oxide (red), benzaldehyde (blue), styrene glycol (grey), benzoic acid (green), phenylacetaldehyde (purple)) concentrations for (b) MIL-101(Cr) and (c) MIL-101(Fe) at 323 K (50 mg catalyst, 50 mL acetonitrile, 50 mmol styrene, 150 mmol H_2O_2). Dashed lines are to guide the eye.

profiles differ between MIL-101(Fe) and MIL-101(Cr), though they both eventually generate benzaldehyde as the majority product by 3600 s and neither catalyst produces detectable amounts of phenylacetaldehyde. Most notably, sustained styrene oxide concentrations are observed over MIL-101(Cr), while any produced over MIL-101(Fe) is quickly consumed after 240 s. After 480 s, product ordering from highest to lowest concentration species stabilizes over MIL-101(Fe) (benzaldehyde > benzoic acid > styrene glycol > styrene oxide). In contrast, the product profile for MIL-101(Cr) switches at 1800 s, which coincides with a change from a clear to a purple tinted reaction broth. Before 1800 s, MIL-101(Cr) only produces styrene oxide and benzaldehyde whereas after 1800 s, styrene glycol and benzoic acid are observed with product ordering settling to: benzaldehyde > styrene glycol > styrene oxide > benzoic acid at 3600 s. We postulate that the change in product distribution on MIL-101(Cr) and the concurrent color changes suggest leached Cr complexes that are catalytically active, which is further discussed in the following section.

We note that other products are observed, with the majority being styrene oligomers. Polymerization of styrene occurs readily *via* self-initiation where two styrene molecules, in the absence of stabilizing agents, first form a Diels–Alder dimer followed by hydrogen transfer to another styrene molecule in molecular-assisted homolysis; the resulting two monoradicals then undergo polymerization to form polystyrene.[41,42] However, stabilized styrene conversion in the absence of catalyst is negligible (<1%) at 3600 s and 323 K, suggesting polymerization must be catalyzed by solid acids, or by MIL-101(Fe)/MIL-101(Cr) in this case. Other trace products in the presence of MIL-101(Cr) and MIL-101(Fe)

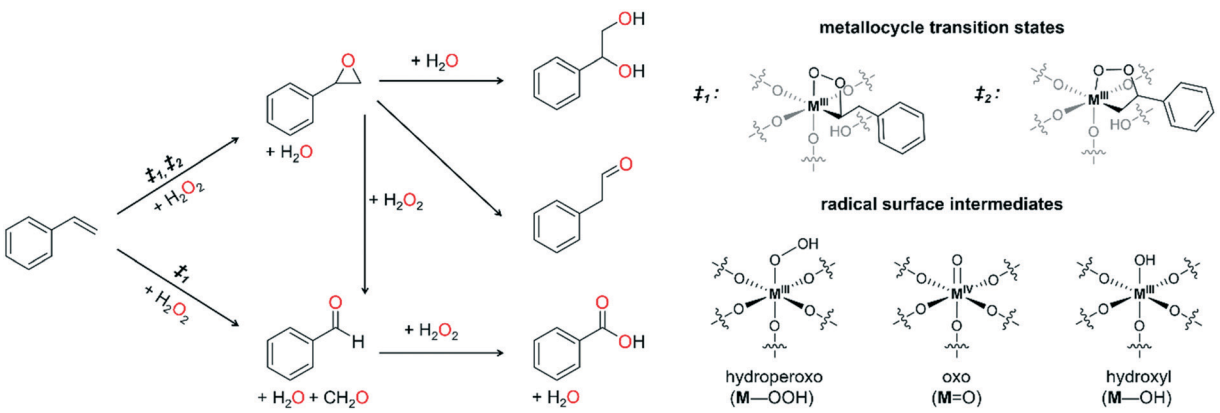

Scheme 1 Proposed reaction pathways, metallocycle transition states, and radical surface intermediates for styrene oxidation by hydrogen peroxide over MIL-101(M).

include various hydrated species from carbonyl-containing compounds and condensation products. However, we focus on the main products that arise from oxidative catalytic turnovers here and in all following discussion, where oxygenate concentration profiles demarcate distinct product distributions by 3600 s for each analog.

We construct a reaction network (Scheme 1) consistent with reported observations to understand the origin of measured oxygenates.[43,44] Direct oxidation of styrene yields styrene oxide and benzaldehyde as primary products, although the nucleophilic attack of hydrogen peroxide on styrene oxide followed by C=C bond cleavage has been reported as an alternate pathway to form benzaldehyde.[17,45] The latter pathway, however, is not prevalent at the reaction conditions studied here. This direct styrene oxidation to form styrene oxide or benzaldehyde is transition metal catalyzed and represents a branch point involving open-site metallocycle transition states (Scheme 1).[46,47] It is not clear from literature whether styrene oxide and benzaldehyde branch from the same 4-member metallocycle transition state ($\ddagger_1$),[17,44] or if they originate from distinct 4- and 5-member ring transition states ($\ddagger_1$ and $\ddagger_2$, respectively).[47] We note that there is another conformer of $\ddagger_2$ wherein styrene interacts through its β carbon to the aromatic ring instead of the α carbon as drawn in Scheme 1, but this structure is not well-reported.

To rationalize the disparate primary product selectivity between MIL-101(Cr) and MIL-101(Fe) (Fig. 4b and c), we first explore H_2O_2-derived radical intermediates leading to metallocycle formation. Metal-bound species that reportedly form from transition metal interactions with H_2O_2 include superoxide ($O_2^{-\bullet}$)/hydroperoxo ($HOO^{\bullet}$) formed from hydrogen abstraction, oxo (O) formed from oxygen abstraction or the cleavage of superoxide/hydroperoxo species, and hydroxyl ($HO^{-\bullet}$) formed from homolytic O–O bond cleavage, but are often experimentally difficult to quantify because they are short-lived.[44,47–51] Rates of superoxide/hydroperoxo formation should be higher on MIL-101(Cr) than MIL-101(Fe) since Cr has a lower Pauling electronegativity (1.66) compared to Fe (1.83), which can result in a lower barrier for radical formation. Transition metal oxo formation is related to oxophilicity, or the tendency of a metal species to form an oxide by oxygen abstraction from or hydrolysis of another species. Oxophilicities (a scale of 0–1) calculated utilizing density functional theory (DFT) on diatomic metal–oxygen molecules utilizing sulfur as a reference ligand indicate that Fe (0.4) is less oxophilic than Cr (0.6),[52] suggesting that there is a larger energy barrier associated with forming metal-oxo intermediates on isolated Fe sites compared to Cr. Finally, hydroxyl radicals are known to form rapidly through homolytic O–O bond cleavage of H_2O_2 on Fe(II), which acts as a reducing agent in a Fenton-like reaction scheme,[48] and on Cr(III),[44] suggesting similar energy barriers on each metal.

These differences in metal electronegativity and oxophilicity suggest lower energy barriers for formation of superoxide/hydroperoxo and oxo on Cr sites compared to on Fe sites, while hydroxyl radical formation occurs similarly in the presence of both. It is the reactivity of these intermediates, however, that confers the observed differences in reactivity for styrene oxidation and in product selectivities between MIL-101(Cr) and MIL-101(Fe). Specifically, oxophilic character suggests that oxygen abstraction or superoxide/hydroperoxo hydrolysis is more facile for Cr than for Fe, which is supported by lower enthalpies of formation for the former calculated *via* DFT.[53] However, high valent Fe-oxo (Fe(IV)=O) is well known to be proficient at abstracting hydrogen atoms from strong C–H bonds.[53,54] For example, Fe(IV)=O has a lower calculated apparent energy barrier than Cr(IV)=O for apolar C–H activation in methane.[53] In this work, Fe(IV)=O serves to activate C–H bonds in styrene, leading to styrene oxide or benzaldehyde. Pseudo first-order reaction rates normalized by initial catalyst mass loadings and by moles of metal over MIL-101(Fe) are indeed higher than those over MIL-101(Cr), which suggests that oxophilic Cr leads to more high valent Cr(IV)=O species that are less active overall for oxidation compared to formed Fe(IV)=O. Superoxide/hydroperoxo species contribute to higher styrene oxide selectivities while hydroxyl radicals yield carbonyl species like benzaldehyde in acetonitrile.[44] This suggests that Cr–OOH, stabilized in comparison to Fe–OOH due to the lower electronegativity of Cr, is largely responsible for the higher styrene oxide selectivity observed for MIL-101(Cr) compared to that for MIL-101(Fe) since this species is more adept at C–H and O–H activation compared to Cr(IV)=O.[55] Further, more electrophilic M–OOH intermediates reportedly confer greater epoxide selectivity,[49] indicating that the electrophilic nature of Cr–OOH is greater than that of Fe–OOH, leading to enhanced epoxide formation.

Beyond primary oxygenate production, Scheme 1 also denotes that styrene oxide can undergo ring-opening isomerization or hydration to yield phenylacetaldehyde or styrene glycol, respectively, while benzaldehyde can react further *via* deep oxidation by hydrogen peroxide to form benzoic acid. Phenylacetaldehyde, formed from the isomerization of styrene oxide, is not observed due to the large presence of water in the reaction broth that facilitates hydration reactions at these reaction conditions. This water is predominantly from the initial charge of 30% aqueous hydrogen peroxide in addition to that generated as an oxidation byproduct, but can also be formed *via* hydrogen peroxide decomposition if higher reaction temperatures are used. Since there is a branch point at primary oxygenate production after which secondary conversions occur in their respective branches, we also consider composite pathways for MIL-101(Cr) and MIL-101(Fe) to understand overall flux toward each branch. Both analogs have a higher selectivity for pathways stemming from benzaldehyde than for those from styrene oxide, but MIL-101(Fe) is at least 10% more selective than MIL-101(Cr) for benzaldehyde pathways. This is overwhelmingly apparent by 3600 s, as MIL-101(Fe) selectively favors benzaldehyde pathways (0.797 ± 0.087) over styrene oxide pathways (0.203 ± 0.024), whereas MIL-101(Cr)

does not discern between benzaldehyde pathway products (0.558 ± 0.128) and styrene oxide pathway products (0.442 ± 0.105) to the same degree. This difference in branch preference further supports that there are underlying electronic differences between each metal.

Examining the proclivity of each catalyst for further oxidation of primary products reveals that neither favors deep oxidation of benzaldehyde to benzoic acid, with benzaldehyde:benzoic acid fractions of more than 1.4 for MIL-101(Cr) and MIL-101(Fe) at all relevant time points, which is consistent with literature that report minor benzoic acid formation from benzaldehyde.[17] Both, however, eventually prefer hydration of styrene oxide to form styrene glycol with styrene oxide:styrene glycol fractions of 0.58 for MIL-101(Cr) and 0 for MIL-101(Fe) at 3600 s. This complete conversion of styrene oxide to styrene glycol on MIL-101(Fe) while MIL-101(Cr) is able to stabilize and turnover styrene oxide is inconsistent with quantitative metal oxophilicity (Cr = 0.6 and Fe = 0.4),[52] which suggests MIL-101(Cr) should be more proficient at activating the epoxide.[11]

Since oxophilicity alone cannot explain differences between MIL-101(Cr) and MIL-101(Fe) tendencies to hydrate styrene oxide, the existence of additional sites is explored. In particular, acid and base densities of as-synthesized samples are quantified *via* temperature programmed desorption (TPD) of NH_3 and CO_2, respectively. We note that NH_3 and CO_2 do not selectively bind to only Lewis or Brønsted sites, primarily because both molecules are small and are therefore able to interact with both sites. However, desorption temperatures can inform relative site strengths, so these temperature-resolved site densities are reported along with total acid and base site densities in Table 1. Acid sites that we attribute to coordinatively unsaturated Fe(II) (ρ_2) and Fe(III) (ρ_3) sites desorb NH_3 at higher temperatures and are more abundant than coordinatively unsaturated Cr(III) sites (ρ_3). Distributions of Fe(II) and Fe(III) sites have been observed in similar Fe-carboxylate MOFs *via* Mössbauer spectrometry and X-ray photoelectron spectroscopy;[56,57] these two Fe oxidation states have reportedly different reactivities for oxidant activation[56] and hydrocarbon oxidation.[57,58] Thus, despite similar NH_3 desorption temperatures for ρ_2 and ρ_3 (Fig. S12a†), they are reported separately here, though we note that multivalency in MIL-101 is neither well-understood nor irrefutably evidenced.[59] Additional sites that desorb NH_3 at lower temperatures (ρ_1) and are likely associated with coordinated oxygen species for both catalysts are more abundant in MIL-101(Fe). Overall, total acid site density for MIL-101(Fe) (12.62 ± 4.35 mmol g_{cat}^{-1}) is more than double that for MIL-101(Cr) (5.57 ± 1.66 mmol g_{cat}^{-1}), consistent with the tendency of MIL-101(Fe) to facilitate styrene oxide hydration to styrene glycol, as this pathway is catalyzed by both Lewis and Brønsted acids. Lewis and Brønsted bases can also catalyze the hydration of styrene oxide to styrene glycol. Total basic site density, comprised of postulated hydroxyl (ρ_4), oxo (ρ_5), and coordinatively unsaturated metal (ρ_6) species, is comparable between MIL-101(Fe) (1.57 ± 0.59 mmol g_{cat}^{-1}) and MIL-101(Cr) (1.63 ± 0.52 mmol g_{cat}^{-1}). Basic site strengths are also similar between the two analogs. While these sites further aid in the conversion of styrene oxide to styrene glycol, the disparity in acid site strength and abundance appears more important in rationalizing the higher proclivity of MIL-101(Fe) to hydrate styrene oxide.

Cycling experiments highlight changes in styrene conversion and oxygenate selectivity profiles

Stability and reusability are key considerations in the design of heterogeneous catalysts to not only promote green chemistry, but also to determine industrial applicability; thus, we probe catalyst deactivation and reactivation potential. Here, we describe catalyst deactivation quantitatively by focusing on single-time point conversion, oxygenate production rates, and product selectivities to observe how catalytic activity changes in each progressing cycle. Fractional styrene conversion (Fig. 5a) decreases with each cycle for both MIL-101(Fe) and MIL-101(Cr), primarily due to observed material losses incurred from solid recovery *via* centrifugation after each cycle and, to a lesser extent, from acetonitrile and ethanol reactivation washings. We note that cycle 1 conversions over fresh material are 60% higher than temporal conversion points at 3600 s because catalyst concentrations in the scaled-up (temporal) reaction broths are lower than those in the smaller batch studies; however, mass-normalized styrene consumption rates are the same order of magnitude from both experimental setups. That being said, calculated instantaneous oxygenate formation rate trends (Fig. 5b) differ between the two materials. For MIL-101(Fe), these rates are relatively consistent between cycles when normalized by recovered catalyst mass, with a 13.2% decrease from cycle 1 (1.97 ± 0.10 mM oxygenates per $g_{catalyst}$ s; 50.1 $mg_{catalyst}$) to cycle 2 (1.71 ± 0.13 mM oxygenates per $g_{catalyst}$ s; 37.7 $mg_{catalyst}$) and a 10.5% decrease from cycle 2 to cycle 3 (1.53 ± 0.08 mM oxygenates per $g_{catalyst}$ s; 17.0 $mg_{catalyst}$). This suggests that there is some site

Table 1 Mass normalized acidic site (ρ_1–ρ_3) and basic site (ρ_4–ρ_6) densities for fresh MIL-101(M) as determined by NH_3-TPD and CO_2-TPD, respectively. Value in parenthesis is the desorption temperature, determined from the center of curve-fitted peaks

M	ρ_1	ρ_2	ρ_3	$\rho_{acid,total}$	ρ_4	ρ_5	ρ_6	$\rho_{base,total}$
	mmol NH_3 g_{cat}^{-1} (K)			mmol NH_3 g_{cat}^{-1}	mmol CO_2 g_{cat}^{-1} (K)			mmol CO_2 g_{cat}^{-1}
Cr	0.68 ± 0.29 (440)	—	4.89 ± 1.63 (544)	5.57 ± 1.66	0.13 ± 0.05 (368)	0.18 ± 0.08 (468)	1.32 ± 0.51 (546)	1.63 ± 0.52
Fe	1.47 ± 0.63 (438)	1.21 ± 0.53 (566)	9.94 ± 4.26 (580)	12.62 ± 4.35	0.07 ± 0.03 (365)	0.13 ± 0.06 (442)	1.37 ± 0.58 (549)	1.57 ± 0.59

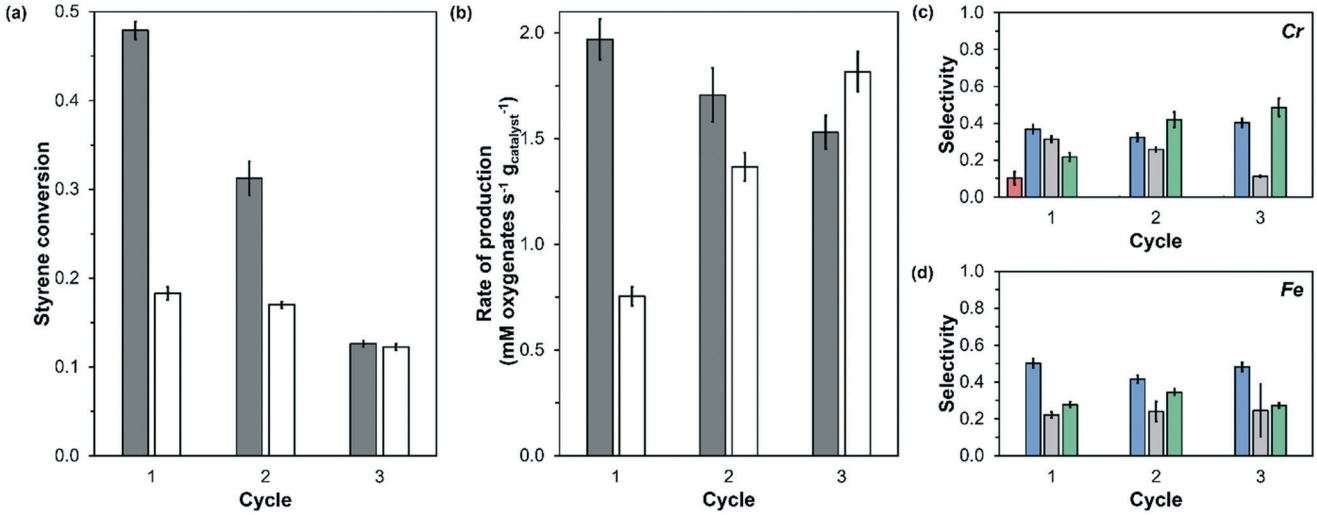

Fig. 5 (a) Fractional styrene conversion for each cycle (grey: Fe, white: Cr), (b) instantaneous rate of total oxygenate production (grey: Fe, white: Cr), and fractional oxygenate selectivity (styrene oxide (red), benzaldehyde (blue), styrene glycol (grey), benzoic acid (green)) at 323 K, 3600 s over (c) MIL-101(Cr) and (d) MIL-101(Fe).

deactivation, but that the nature of sites in MIL-101(Fe) does not change drastically between catalytic cycles and observed losses in conversion are largely due to solid transfer losses. In contrast, MIL-101(Cr) rates increase between cycles with an 82.7% increase from cycle 1 (0.75 ± 0.05 mM oxygenates per $g_{catalyst}$ s; 49.9 $mg_{catalyst}$) to cycle 2 (1.37 ± 0.07 mM oxygenates per $g_{catalyst}$ s; 25.6 $mg_{catalyst}$) and a 32.8% increase from cycle 2 to cycle 3 (1.82 ± 0.10 mM oxygenates per $g_{catalyst}$ s; 13.9 $mg_{catalyst}$), despite lower styrene conversions. This indicates that, in addition to solid losses, there are other deactivation phenomena present, such as Cr leaching, which is consistent with the light purple color of the reaction broth after solid removal.

Further, both analog broths exhibit small concentrations (10^{-4} M) of the BDC linker, as ^{1}H NMR spectroscopy is sufficiently sensitive for detection at those concentrations. MIL-101(Fe) only shows evidence of linker leaching in cycle 1, whereas MIL-101(Cr) exhibits leaching in all three cycles (Fig. S16b†). Linker leaching for MIL-101(Fe) may also persist for cycles 2 and 3 but exist in concentrations below ^{1}H NMR detection limits (10^{-9} M) and are thus unambiguously lower than linker leaching in MIL-101(Cr). The mole fraction of leached BDC for the Cr analog is nearly 1.5 times that of its Fe counterpart in cycle 1. This BDC is unlikely to be residual starting material left from synthetic methods, as a singlet at 8.04 ppm in ^{1}H NMR for the aromatic hydrogens on BDC is not observed for either catalyst after 3600 s at 323 K in neat acetonitrile (Fig. S16a†). Additionally, a peak at 17.7° 2θ (ref. 60) in XRD diffractograms for crystalline BDC with long-range order is not observed for fresh MIL-101(Cr) or MIL-101(Fe). Thus, the detected BDC is reasonably attributed to linker leaching during the catalytic experiments, which is consistent with oxygenate production rate trends (Fig. 5b), as the largest decrease in rates is between cycle 1 and cycle 2 for MIL-101(Fe) and large increases in rates are observed between all three cycles for MIL-101(Cr).

Product selectivities for the main products (styrene oxide, benzaldehyde, styrene glycol, and benzoic acid) at 3600 s are also recorded for each cycle for both analogs at 323 K (Fig. 5c and d). It is apparent that fresh (cycle 1) MIL-101(Cr) and MIL-101(Fe) show different product distributions at 3600 s, consistent with temporal concentration profile trends. Considering primary products from the initial oxidation event of styrene, MIL-101(Cr) has a higher selectivity to benzaldehyde (0.368 ± 0.131) over styrene oxide (0.102 ± 0.035) at 3600 s. At the same time point, MIL-101(Fe) also prefers benzaldehyde as its majority primary product (0.502 ± 0.037), but no styrene oxide is observed. The observed proclivity of both analogs to generate benzaldehyde as the majority oxygenate by 3600 s is consistent with other studies at mild temperatures below 373 K that observe benzaldehyde as the major oxygenate product from styrene oxidation by hydrogen peroxide over transition metal catalysts, including Cr- and Fe-based materials.[17,61,62]

For overall process sustainability, it is paramount to understand reactivity and selectivity not only as functions of chemical and electronic properties, but also as functions of their evolution in several reaction cycles. After the first cycle at 323 K, reactivated MIL-101(Cr) and MIL-101(Fe) show different product distributions compared to one another, though these differences are subtler in cycles 2 and 3. The assertion that MIL-101(Fe) site nature does not change drastically from cycle to cycle is upheld, as the product profile (benzaldehyde > benzoic acid > styrene glycol) is maintained within error. In contrast, MIL-101(Cr) shows a clear change in its product profile, notably in the apparent loss of its ability to form styrene oxide after cycle 1. Additionally, the deep oxidation of benzaldehyde to form benzoic acid becomes favored in cycles 2 and 3, which is not

observed for MIL-101(Fe). These changes coincide with increased rates, despite decreases in conversion, and Cr leaching with each cycle. Altogether, these observations support that the leached Cr species are indeed catalytically active and have consequences for product selectivity. This is further confirmed by hot filtration tests (Fig. S17 and S18†) where solvated Cr complexes remaining in the reaction broth after MIL-101(Cr) solid removal are allowed to react at 323 K for another 3600 s; these complexes continue to catalyze styrene oxidation and affect product distributions by increasing selectivity to benzoic acid over benzaldehyde and showing no selectivity for styrene oxide. In contrast, hot filtration tests over MIL-101(Fe) show negligible changes in styrene conversion, turnover rates, and product distribution after solid removal, supporting the conclusion that MIL-101(Fe) operates as a heterogeneous catalyst (Fig. S19 and S20†).

Characterizing key changes in physicochemical properties after recycling experiments

To complement catalytic experiments, SEM, XRD, and FT-IR and UV-vis spectroscopies probe changes in textural and electronic properties after reaction. Specifically, SEM images are taken after cycle 3, but before reactivation procedures, to observe any changes in aggregate morphology after reaction (Fig. 6a and b). Both materials show no evidence of catastrophic collapse of aggregate structure and retain some qualitative semblance to fresh samples (Fig. 2c and d).

FT-IR spectroscopy probes both materials further after reaction and reactivation and the resulting spectra (Fig. 6c and d) assert that there are changes in surface functionality in both materials. Characteristic band intensities in the fingerprint region at lower wavenumbers notably decrease after reaction for both analogs, indicating that reaction conditions change the nature of the MOF surfaces. Specifically, the loss of bands assigned to C=C and C–H vibrations suggests that the nature of the BDC backbone has changed, most likely through involvement in catalytic turnovers or through interactions with hydrogen peroxide and not due to the thermal effects, as these bands remained visible after exposure to neat solvent at reaction temperature (Fig. S10†). In contrast, bands indicative of O–C–O functionalities, also belonging to the BDC framework backbone, remain in both MIL-101(Fe) and MIL-101(Cr), although the shape of these bands changes. Band-broadening, like in the case of MIL-101(Cr), or changes in relative intensity between O–C–O bands, as is the case with both analogs, suggest interactions between the reactants or products with the organic backbone that are mitigated to differing degrees by reactivation procedures. Specifically, spectra before and after reactivation washings appear similar to one another but distinctly different from the fresh spectra for MIL-101(Cr), whereas there is a marked difference in O–C–O bands for MIL-101(Fe) before and after reactivation. This suggests that MIL-101(Fe) is more receptive to the reported reactivation procedures and different strategies need to be utilized for MIL-101(Cr).

XRD patterns of spent materials after just one cycle (Fig. S9†) reveal the loss of low angle characteristic peaks for both MIL-101(Cr) and MIL-101(Fe), possibly implicating severe pore occlusion, partial pore collapses, and subtle structural disordering during catalytic turnovers as possible deactivation mechanisms. A reduction in BET surface areas after reaction combined with PSD broadening in the mesoporous range commiserate with a loss of microporosity (Fig. S8†) implicate the first two phenomena for both MIL-101(Cr) and MIL-101(Fe). The last phenomena could be caused by metal or linker leaching or a combination of the two. Consistent with literature,[29] we observe that Cr leaching

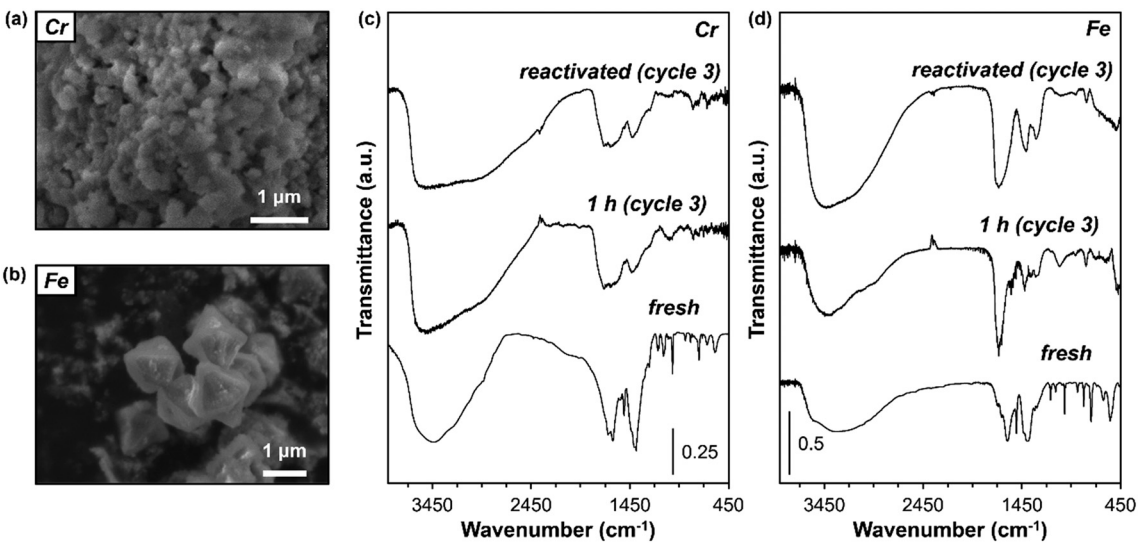

Fig. 6 SEM images of spent (cycle 3, no reactivation) (a) MIL-101(Cr) and (b) MIL-101(Fe). FT-IR spectra of fresh, spent (cycle 3), and reactivated (cycle 3) (c) MIL-101(Cr) and (d) MIL-101(Fe).

is also exacerbated by interactions with hydrogen peroxide as evidenced by UV-vis spectra (Fig. S11b†) of the visibly purple broth after exposure to 10 mL acetonitrile and 30 mmol aqueous hydrogen peroxide at 323 K for 3600 s in the absence of styrene. Characteristic diffraction peaks do not reappear after reactivation procedures for both analogs, but this may also be due to the small amount of sample (on the order of 30 mg) remaining after such procedures. We note that the lack of characteristic peaks in XRD patterns after reactivation procedures can coexist with FT-IR observations if oxidative events during reaction induce mild degrees of pore collapse or restructuring that are not significant enough to eliminate local structure and detectable functionality in FT-IR spectra, but are large enough that the distortion of long-range structure results in an "amorphous" XRD pattern. In all, neither analog suffered complete structural collapse. Instead, both show changes in surface functionality of differing reactivation potential, where MIL-101(Fe) demonstrates a higher susceptibility to this set of reactivation procedures compared to MIL-101(Cr).

Motivated by the observed changes in surface chemistry, UV-vis is used to further probe changes in electronics after reaction. Fresh MIL-101(Fe) (Fig. 7b) has two distinguishable features: a sharper peak at 290 nm that can be attributed to a ligand-centered transition of the BDC linker and a broader feature centered around 400 nm attributed to the ligand to metal charge transfer (LMCT) band. After reaction at 323 K, the LMCT band disappears, confirming that the species associated with this electronic transition, notably the coordinated Fe center, is involved in catalytic turnovers. This species shows a degree of reactivation, as washing and drying procedures described in this work result in the re-emergence of the LMCT band. This observation complements FT-IR spectra (Fig. 6d), showing that Fe species can also be regenerated after reactivation procedures in addition to some O–C–O functionalities in the linker backbone. A parallel UV-vis analysis for MIL-101(Cr) could not be performed because the solid aggregates are too large and do not form a suspension in acetonitrile or other solvents on the timescale needed for these measurements. However, liquid-phase UV-vis confirms the presence of solvated Cr(III) species,[63] likely $[Cr(H_2O)_6]^{3+}$ given the large presence of water in the reaction broth, that have leached from the framework into the broth during reaction at 323 K (Fig. 7a). The amount of solvated Cr in the reaction broth increases with each subsequent reaction cycle, suggesting that defects in the crystal structure caused by metal leaching in each preceding cycle catalyzes further degradation. The MIL-101(Fe) broth after reaction appears clear with a yellow hue, suggesting Fe leaching, which is consistent with literature.[29] However, leached Fe species do not have significant implications for catalysis, as hot filtration tests (Fig. S19 and S20†) show no further styrene conversion or changes in product distribution after the solid is removed. Further, relatively constant mass-normalized rates from cycling experiments (Fig. 5b) suggest that leached Fe species from MIL-101(Fe) are not catalytically active. Overall, material characterization findings are consistent with catalytic observations and together, show that although both analogs are active for styrene conversion to form various oxygenate products, the reactivity of Cr and Fe nodes are different, as well as the mechanisms by which the two deactivate and their propensity for reactivation.

Styrene oxidation on both ordered and disordered phases of MIL-101(Cr)

Thus far, we have demonstrated that HF-free hydrothermal MIL-101(Cr) synthesis yielded catalytically active, albeit relatively unstable, MIL-101(Cr) that was comparatively studied with isostructural MIL-101(Fe). However, unlike MIL-101(Fe), three chromatically distinguishable phases (Fig. S1a†) were observed upon synthesis: a light green (hex: #8BA194) phase with the lowest density, a grey (hex: #9B928C) intermediate density phase, and an emerald green (hex: #1F4932) phase with the highest density. Typical yield of these three phases combined is 48% on a Cr basis. There are scant reports on the existence of these three phases from hydrothermal syntheses, let alone their comparative catalytic efficacies, but acid mineralizing agents such as hydrofluoric acid and nitric acid, have been shown to produce single MIL-101 phases.[23,64] The highest density phase was the subject for comparison with MIL-101(Fe) in previous sections, but

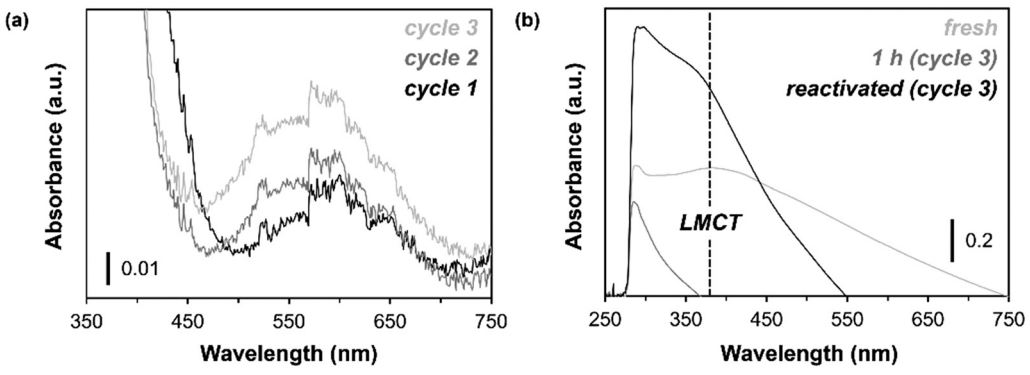

Fig. 7 Liquid-phase UV-vis spectra at ambient temperature of (a) reaction broth after MIL-101(Cr) solid removal for each cycle and of (b) suspended fresh, spent (cycle 3), and reactivated MIL-101(Fe) in acetonitrile.

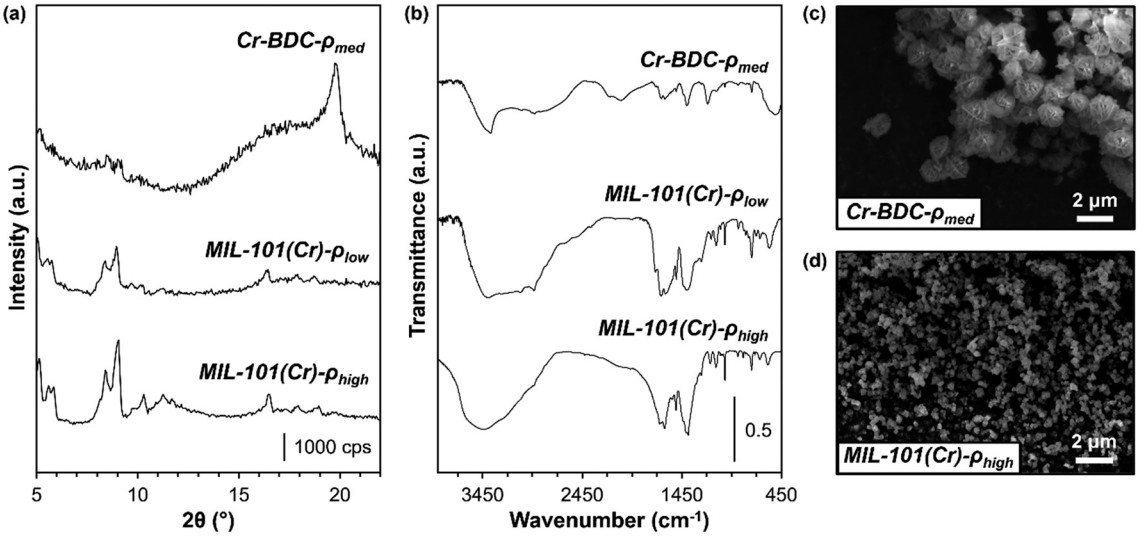

Fig. 8 (a) XRD patterns and (b) FTIR spectra of MIL-101(Cr)-ρ_{low}, Cr-BDC-ρ_{med}, MIL-101(Cr)-ρ_{high}. SEM images of (c) Cr-BDC-ρ_{med} and (d) MIL-101(Cr)-ρ_{low}. The SEM image for MIL-101(Cr)-ρ_{high} at the same magnification is in Fig. 2d.

despite its activity for styrene oxidation, this phase suffers from Cr leaching. As such, we investigate these three Cr phases to elucidate textural differences and impacts on catalytic activity.

XRD patterns (Fig. 8a) show that the lowest density phase, termed MIL-101(Cr)-ρ_{low}, exhibits all characteristic MIL-101 peaks compared to the highest density phase, termed MIL-101(Cr)-ρ_{high}. The intermediate density phase, however, lacks most characteristic MIL-101 peaks except for very weak twin peaks in the 8–9° 2θ range and is appropriately termed Cr-BDC-ρ_{med}. Further, there is a peak at 19.8° 2θ, which is not consistent with MIL-101, Cr oxides, or Cr carbides, that provides support for the hypothesis that this is a unique phase.[64] This unique phase (Cr-BDC-ρ_{med}) is postulated to be a transitionary phase between MIL-101 and MIL-53 (a higher density microporous Cr carboxylate) that forms from the degradation of MIL-101 at longer synthesis times.[65] Though rearrangement of these decomposed species forms MIL-53,[65] Cr-BDC-ρ_{med} does not exhibit any characteristic MIL-53 XRD peaks (Fig. S14b†), further supporting that this phase is transitionary.

FT-IR spectra (Fig. 8b) complement XRD patterns, where all bands for MIL-101(Cr)-ρ_{low} and MIL-101(Cr)-ρ_{high} suggest similar surface functionalities characteristic of MIL-101(Cr). Cr-BDC-ρ_{med} retains some MIL-101(Cr) functionality, especially strong O–C–O bands between 1400–1600 cm^{-1}, but exhibits lower overall transmittance with peak broadening compared to MIL-101(Cr)ρ_{low} and MIL-101(Cr)-ρ_{high}, supporting its transitionary, disordered structure. From SEM images, MIL-101(Cr)-ρ_{low} (Fig. 8d) is comprised of octahedral crystals with an average diameter of 0.32 ± 0.05 μm, which is comparable in size to those observed in MIL-101(Cr)-ρ_{high} (0.31 ± 0.09 μm), though the higher density MIL-101 crystals are qualitatively more irregular in shape, quantitatively reflected in a wider particle size distribution (Fig. S4†) for MIL-101(Cr)-ρ_{high}. Cr-BDC-ρ_{med} particles (Fig. 8c) deviate significantly from the structure and size of MIL-101(Cr) and instead are much larger (1.6 ± 0.2 μm), spherical, and have a needle-like substructure, reminiscent of yarn balls. From these textural characterizations, it is apparent that MIL-101(Cr)-ρ_{low} and MIL-101(Cr)-ρ_{high} show similar bulk and surface properties with subtle differences, but both differ significantly from Cr-BDC-ρ_{med} and these differences have an impact on catalytic activity.

Single-time point (3600 s, 323 K) experiments followed by hot filtration leaching tests demonstrate that styrene conversion by hydrogen peroxide differs among MIL-101(Cr)-ρ_{low}, Cr-BDC-ρ_{med}, and MIL-101(Cr)-ρ_{high}. We first acknowledge that the styrene conversion here (Fig. 9) for MIL-101(Cr)-ρ_{high} is 41.8% of that in Fig. 5a. This is due to a lower Cr mole percent in the batch used in this experiment

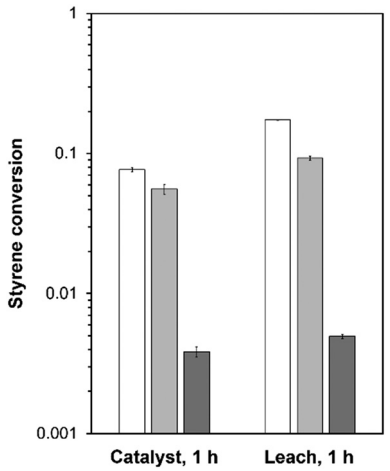

Fig. 9 Styrene conversion for MIL-101(Cr)-ρ_{high} (white), Cr-BDC-ρ_{med} (light grey), and MIL-101(Cr)-ρ_{low} (dark grey) at 3600 s (1 h), and 323 K. Styrene conversion before reaction is 0.0039 ± 0.0001.

(3.6 at%) compared to the one in Fig. 5a (12.8 at%), though normalized oxygenate production rates representing a lower bound where all Cr species are considered active are on the same order of magnitude (this batch: 6.30 ± 0.36 mM oxygenates per s mmol Cr, Fig. 5a: 4.23 ± 0.25 mM oxygenates per s mmol Cr). Here, we emphasize that properly normalized rates can overcome differences in metal content between syntheses and instead provides insight into the intrinsic activity of Cr sites in each sample. Notably, the oxygenate production rate normalized by Cr content for MIL-101(Cr)-ρ_{low} (0.19 ± 0.02 mM oxygenates per s mmol Cr) is lower than those of Cr-BDC-ρ_{med} (0.96 ± 0.09 mM oxygenates per s mmol Cr) and MIL-101(Cr)-ρ_{high} (6.30 ± 0.36 mM oxygenates per s mmol Cr) with styrene conversions over MIL-101(Cr)-ρ_{low} being an order of magnitude lower than those of Cr-BDC-ρ_{med} and MIL-101(Cr)-ρ_{high}. This is not an intuitive result in the case of MIL-101(Cr)-ρ_{low} and MIL-101(Cr)-ρ_{high}, as textural characterization suggests that they have similar properties. However, if we consider elemental composition, MIL-101(Cr)-ρ_{low} has a higher Cr mole percentage (6.0 at%) compared to MIL-101(Cr)-ρ_{high} (3.6 at%), the former being within error compared to the theoretical 5 at% Cr (7 at% for EDXS that does not detect H) for the nominal chemical formula of $[Cr_3(O)(OH)(BDC)_3(H_2O)_2]$ for defect-free MIL-101(Cr). This, together with lower styrene conversion and oxygenate production rates over MIL-101(Cr)-ρ_{low}, suggests that MIL-101(Cr)-ρ_{high} contains a higher density of active Cr species, potentially from defects from incomplete Cr trimers. Enhanced adsorption and catalytic activity on open active sites have been observed for other transition metal carboxylate MOFs with defects caused by missing linkers, metal sites, or both.[66–68] Defects are further implicated by the higher styrene conversion exhibited by the disordered Cr-BDC-ρ_{med} compared to MIL-101(Cr)-ρ_{low}. We note that the defects in fresh MIL-101(Cr)-ρ_{high} are randomly distributed and are scarce enough not to impact overall long-range crystal structure or functionality assessed by XRD and FT-IR, respectively. Further, defect density is challenging to control and quantify, and this is reflected by the varying Cr mole fractions of MIL-101(Cr)-ρ_{high} batches mentioned earlier. Cr-trimer defects are further supported by the observation of a purple reaction broth (Fig. S11a†), indicating leached Cr species, after 3600 s of reaction for MIL-101(Cr)-ρ_{high} and Cr-BDC-ρ_{med}, but not for MIL-101(Cr)-ρ_{low}. These leached species are again confirmed to be active for styrene oxidation with a 114.5% increase in styrene conversion for MIL-101(Cr)-ρ_{high} and a 66.1% increase for Cr-BDC-ρ_{med} after hot filtration.

Though defects are postulated to increase styrene conversion, Cr-BDC-ρ_{med} and MIL-101(Cr)-ρ_{high} show different product distributions, indicating that the MIL-101 crystalline structure has important implications for oxygenate selectivity. Styrene oxide production is observed over MIL-101(Cr)-ρ_{high} but not over disordered Cr-BDC-ρ_{med}, which produces benzaldehyde (0.023 ± 0.005), styrene glycol (major product, 0.747 ± 0.175), and benzoic acid (0.230 ± 0.054) but no styrene oxide. This suggests that the coordination environment around Cr in crystalline MIL-101 affords electronic properties that enable desorption of styrene oxide rather than complete hydration to styrene glycol. Overall, we observed three distinct materials produced from HF-free hydrothermal MIL-101(Cr) synthesis that demonstrated differing efficacies for styrene oxidation due in part to Cr trimer defects and different coordination environments.

Conclusion

For styrene oxidation by H_2O_2, temporal and single-time point recyclability experiments assert that compared to MIL-101(Cr), MIL-101(Fe) is more reactive, recyclable, and pathway selective, with a higher preference for primary aldehyde (benzaldehyde) formation over epoxide (styrene oxide) formation. Reactivity and selectivity differences between MIL-101(Fe) and MIL-101(Cr) are rooted in relative ability to form reactive radical intermediates from H_2O_2 and open-site metallocycle transition states. Oxidation by H_2O_2 often implicates reactive surface-bound radical intermediates, M(III)–OOH, M(III)–OH, and high valent M(IV)═O. Oxophilicity suggests that oxygen abstraction to form M═O is more facile for Cr, but the higher reactivity of Fe(IV)═O to activate C–H bonds translates to the higher observed styrene oxidation for MIL-101(Fe). Meanwhile, a lower electronegativity allows Cr sites to better stabilize reactive M(III)–OOH radicals after initial hydrogen abstraction; the higher electrophilicity of formed Cr(III)–OOH confers increased styrene oxide selectivity compared to MIL-101(Fe). Secondary conversions occur over both analogs, forming styrene glycol through ring-opening styrene oxide hydration and benzoic acid through deep oxidation of benzaldehyde by H_2O_2. The former pathway is more prevalent for MIL-101(Fe) than for MIL-101(Cr), consistent with a higher acid site density on MIL-101(Fe). Catalyst recyclability experiments complemented by various characterization techniques determine that MIL-101(Fe) sites are more regenerable utilizing the mild reactivation procedures reported in this work whereas MIL-101(Cr) suffers from metal leaching that impacts oxygenate production rates and selectivities and is not regenerable to a significant degree. Lastly, styrene turnover rates for three chromatically unique phases of MIL-101(Cr) obtained for a single synthesis suggest that Cr-trimer defects resulting in open active sites contained in MIL-101 crystalline pores are largely responsible for observed reactivity and selectivity, but increase framework susceptibility to deactivation *via* metal or linker leaching. Overall, this work rigorously quantifies differing material stabilities, reactivities, and oxygenate selectivities between isostructural MIL-101(Cr) and MIL-101(Fe) as a function of their structural and electronic property differences and the fundamental understanding of catalyst behavior and limitations defined here can be applied to future catalyst design and to other hydrocarbon oxidation reactions that are ubiquitous in modern chemistry industries.

Conflicts of interest

There are no conflicts to declare.

Acknowledgements

This work was supported by start-up funds from Princeton University. The authors acknowledge the use of Princeton's Imaging and Analysis Center, which is partially supported through the Princeton Center for Complex Materials (PCCM), a National Science Foundation (NSF)-MRSEC program (DMR-2011750). The authors also appreciate access to the Department of Chemistry's NMR facility at Princeton that has been instrumental to this work. Finally, the authors also thank Matthew Ko for his assistance in the synthetic efforts to yield MIL-101(Cr).

References

1 Y. Lin, C. Kong and L. Chen, *RSC Adv.*, 2012, **2**, 6417–6419.
2 J. H. Wang, M. Li and D. Li, *Chem. – Eur. J.*, 2014, **20**, 12004–12008.
3 P. Horcajada, C. Serre, G. Maurin, N. A. Ramsahye, F. Balas, M. Vallet-Regí, M. Sebban, F. Taulelle and G. Férey, *J. Am. Chem. Soc.*, 2008, **130**, 6774–6780.
4 Z. Hu, B. J. Deibert and J. Li, *Chem. Soc. Rev.*, 2014, **43**, 5815–5840.
5 D. Sun, Q. Deng and J. Long, *J. Solid State Electrochem.*, 2018, **22**, 487–493.
6 Y. Cui, J. Zhang, H. He and G. Qian, *Chem. Soc. Rev.*, 2018, **47**, 5740–5785.
7 A. Corma, H. García and F. X. Llabrés I Xamena, *Chem. Rev.*, 2010, **110**, 4606–4655.
8 K. Leng, Y. Sun, X. Li, S. Sun and W. Xu, *Cryst. Growth Des.*, 2016, **16**, 1168–1171.
9 A. Dhakshinamoorthy, A. M. Asiri and H. Garcia, *Chem. – Eur. J.*, 2016, **22**, 8012–8024.
10 L. Ma, C. Abney and W. Lin, *Chem. Soc. Rev.*, 2009, **38**, 1248–1256.
11 B. R. James, J. A. Boissonnault, A. G. Wong-Foy, A. J. Matzger and M. S. Sanford, *RSC Adv.*, 2018, **8**, 2132–2137.
12 O. V. Zalomaeva, A. M. Chibiryaev, K. A. Kovalenko, O. A. Kholdeeva, B. S. Balzhinimaev and V. P. Fedin, *J. Catal.*, 2013, **298**, 179–185.
13 J. Kim, S. N. Kim, H. G. Jang, G. Seo and W. S. Ahn, *Appl. Catal., A*, 2013, **453**, 175–180.
14 P. Horcajada, S. Surblé, C. Serre, D. Y. Hong, Y. K. Seo, J. S. Chang, J. M. Grenèche, I. Margiolaki and G. Férey, *Chem. Commun.*, 2007, 2820–2822.
15 J. Tang, M. Yang, M. Yang, J. Wang, W. Dong and G. Wang, *New J. Chem.*, 2015, **39**, 4919–4923.
16 I. Y. Skobelev, A. B. Sorokin, K. A. Kovalenko, V. P. Fedin and O. A. Kholdeeva, *J. Catal.*, 2013, **298**, 61–69.
17 J. Sun, G. Yu, Q. Huo, Q. Kan and J. Guan, *RSC Adv.*, 2014, **4**, 38048–38054.
18 N. V. Maksimchuk, K. A. Kovalenko, V. P. Fedin and O. A. Kholdeeva, *Adv. Synth. Catal.*, 2010, **352**, 2943–2948.
19 B. Ma, W. Zhao, F. Zhang, Y. Zhang, S. Wu and Y. Ding, *RSC Adv.*, 2014, **4**, 32054–32062.
20 Y. Ding, B. Ma, D. Tong, H. Hua and W. Zhao, *Aust. J. Chem.*, 2009, **62**, 739–746.
21 Y. Ding, W. Zhao, H. Hua and B. Ma, *Green Chem.*, 2008, **10**, 910–913.
22 A. Dhakshinamoorthy, M. Alvaro and H. Garcia, *Catal. Sci. Technol.*, 2011, **1**, 856–867.
23 C. Férey, C. Mellot-Draznieks, C. Serre, F. Millange, J. Dutour, S. Surblé and I. Margiolaki, *Science*, 2005, **309**, 2040–2042.
24 O. A. Kholdeeva, *Catal. Today*, 2016, **278**, 22–29.
25 I. D. Ivanchikova, I. Y. Skobelev and O. A. Kholdeeva, *J. Organomet. Chem.*, 2015, **793**, 175–181.
26 F. Farzaneh and Y. Sadeghi, *J. Mol. Catal. A: Chem.*, 2015, **398**, 275–281.
27 D. E. Kravchenko, I. A. Tyablikov, P. A. Kots, B. A. Kolozhvari, D. A. Fedosov and I. I. Ivanova, *Pet. Chem.*, 2018, **58**, 1255–1262.
28 O. A. Kholdeeva, I. Y. Skobelev, I. D. Ivanchikova, K. A. Kovalenko, V. P. Fedin and A. B. Sorokin, *Catal. Today*, 2014, **238**, 54–61.
29 O. Kholdeeva and N. Maksimchuk, *Catalysts*, 2021, **11**, 283.
30 L. Bromberg, Y. Diao, H. Wu, S. A. Speakman and T. A. Hatton, *Chem. Mater.*, 2012, **24**, 1664–1675.
31 D. A. Gómez-Gualdrón, P. Z. Moghadam, J. T. Hupp, O. K. Farha and R. Q. Snurr, *J. Am. Chem. Soc.*, 2016, **138**, 215–224.
32 H. Hu, H. Zhang, Y. Chen and H. Ou, *Environ. Sci. Pollut. Res.*, 2019, **101**, 24720–24732.
33 A. D. Yeganeh, M. M. Amini and N. Safari, *J. Porphyrins Phthalocyanines*, 2019, **23**, 1118–1131.
34 Q. Liu, L. Ning, S. Zheng, M. Tao, Y. Shi and Y. He, *Sci. Rep.*, 2013, **3**, 1–6.
35 E. Rahmani and M. Rahmani, *Front. Chem. Sci. Eng.*, 2020, **14**, 1100–1111.
36 C. S. Inc., *NIST Chemistry WebBook, NIST Standard Reference Database*, National Institute of Standards and Technology, Gaithersburg, MD, 20899, Number 69, 2018.
37 J. Ma, A. P. Kalenak, A. G. Wong-foy and A. J. Matzger, *Angew. Chem., Int. Ed.*, 2017, **56**, 14618–14621.
38 J. E. Mondloch, O. Karagiaridi, O. K. Farha and J. T. Hupp, *CrystEngComm*, 2013, **15**, 9258–9264.
39 A. J. Howarth, A. W. Peters, N. A. Vermeulen, T. C. Wang, J. T. Hupp and O. K. Farha, *Chem. Mater.*, 2017, **29**, 26–39.
40 G. Han, Q. Qian, K. Mizrahi Rodriguez and Z. P. Smith, *Ind. Eng. Chem. Res.*, 2020, **59**, 7888–7900.
41 F. R. Mayo, *J. Am. Chem. Soc.*, 1953, **75**, 6133–6141.
42 K. S. Khuong, W. H. Jones, W. A. Pryor and K. N. Houk, *J. Am. Chem. Soc.*, 2005, **127**, 1265–1277.
43 T. A. G. Duarte, A. C. Estrada, M. M. Q. Simões, I. C. M. S. Santos, A. M. V. Cavaleiro, M. G. P. M. S. Neves and J. A. S. Cavaleiro, *Catal. Sci. Technol.*, 2015, **5**, 351–363.
44 H. Chen, W. Wang, Y. Yang, P. Jiang, W. Gao, R. Cong and T. Yang, *Appl. Catal., A*, 2019, **588**, 117283.

45 V. Hulea and E. Dumitriu, *Appl. Catal., A*, 2004, **277**, 99–106.
46 A. K. Rappé and W. A. Goddard, *Nature*, 1980, **285**, 311–312.
47 Q. Wang, X. Liang, R. Bi, Y. Liu, Y. He, J. Feng and D. Li, *Dalton Trans.*, 2019, **48**, 16402–16411.
48 J. J. Pignatello, E. Oliveros and A. MacKay, *Crit. Rev. Environ. Sci. Technol.*, 2006, **36**, 1–84.
49 D. T. Bregante, N. E. Thornburg, J. M. Notestein and D. W. Flaherty, *ACS Catal.*, 2018, **8**, 2995–3010.
50 D. T. Bregante, J. Z. Tan, R. L. Schultz, E. Z. Ayla, D. S. Potts, C. Torres and D. W. Flaherty, *ACS Catal.*, 2020, **10**, 10169–10184.
51 A. S. Petit, R. C. R. Pennifold and J. N. Harvey, *Inorg. Chem.*, 2014, **53**, 6473–6481.
52 K. P. Kepp, *Inorg. Chem.*, 2016, **55**, 9461–9470.
53 A. S. Rosen, J. M. Notestein and R. Q. Snurr, *Angew. Chem.*, 2020, **132**, 19662–19670.
54 M. C. Simons, J. G. Vitillo, M. Babucci, A. S. Hoffman, A. Boubnov, M. L. Beauvais, Z. Chen, C. J. Cramer, K. W. Chapman, S. R. Bare, B. C. Gates, C. C. Lu, L. Gagliardi and A. Bhan, *J. Am. Chem. Soc.*, 2019, **141**, 18142–18151.
55 J. Cho, J. Woo, J. Eun Han, M. Kubo, T. Ogura and W. Nam, *Chem. Sci.*, 2011, **2**, 2057–2062.
56 M. Pu, Y. Ma, J. Wan, Y. Wang, J. Wang and M. L. Brusseau, *Catal. Sci. Technol.*, 2017, **7**, 1129–1140.
57 A. Dhakshinamoorthy, M. Alvaro, P. Horcajada, E. Gibson, M. Vishnuvarthan, A. Vimont, J. M. Grenèche, C. Serre, M. Daturi and H. Garcia, *ACS Catal.*, 2012, **2**, 2060–2065.
58 J. N. Hall and P. Bollini, *Chem. – Eur. J.*, 2020, **26**, 16639–16643.
59 J. N. Hall and P. Bollini, *React. Chem. Eng.*, 2019, **4**, 207–222.
60 E. Haque, N. A. Khan, J. E. Lee and S. H. Jhung, *Chem. – Eur. J.*, 2009, **15**, 11730–11736.
61 W. Tanglumlert, T. Imae, T. J. White and S. Wongkasemjit, *Catal. Commun.*, 2009, **10**, 1070–1073.
62 D. R. Das, P. Kalita and A. K. Talukdar, *J. Porous Mater.*, 2020, **27**, 893–903.
63 A. Mohammadi, M. M. Doroodmand and M. M. R. Sadegh, *J. Text. Sci. Eng.*, 2016, **6**, 1–6.
64 T. Zhao, F. Jeremias, I. Boldog, B. Nguyen, S. K. Henninger and C. Janiak, *Dalton Trans.*, 2015, **44**, 16791–16801.
65 N. A. Khan and S. H. Jhung, *Cryst. Growth Des.*, 2010, **10**, 1860–1865.
66 R. S. Forgan, *Chem. Sci.*, 2020, **11**, 4546–4562.
67 H. Guo, S. Su, Y. Liu, X. Ren and W. Guo, *Environ. Sci. Pollut. Res.*, 2020, **27**, 17194–17204.
68 J. Wang, L. Liu, C. Chen, X. Dong, Q. Wang, L. Alfilfil, M. R. Alalouni, K. Yao, J. Huang, D. Zhang and Y. Han, *J. Mater. Chem. A*, 2020, **8**, 4464–4472.

